Ore Geology Reviews 79 (2016) 367–381

Contents lists available at ScienceDirect

Ore Geology Reviews

journal homepage: www.elsevier.com/locate/oregeorev

Origin of nelsonite and Fe–Ti oxides ore of the Damiao anorthosite complex, NE China: Evidence from trace element geochemistry of apatite, plagioclase, magnetite and ilmenite

Hai-Long He [a,b], Song-Yue Yu [a], Xie-Yan Song [a,*], Zhi-Song Du [c], Zhi-Hui Dai [a], Ting Zhou [a], Wei Xie [d]

[a] State Key Laboratory of Ore Deposit Geochemistry, Institute of Geochemistry, Chinese Academy of Sciences, Guiyang 550002, PR China
[b] University of Chinese Academy of Sciences, Beijing 100049, PR China
[c] The 4th Geological Team of Hebei Geology and Mining Bureau, Chengde 067000, PR China
[d] State Key Laboratory of Isotope Geochemistry, Guangzhou Institute of Geochemistry, Chinese Academy of Sciences, Guangzhou 510640, PR China

ARTICLE INFO

Article history:
Received 18 December 2015
Received in revised form 30 May 2016
Accepted 31 May 2016
Available online 8 June 2016

Keywords:
Nelsonite
Fe–Ti oxides ore
Damiao anorthosite complex
Liquid immiscibility
Magma chamber processes
North China craton

ABSTRACT

Nelsonite and Fe–Ti oxides ore are common in Proterozoic massif-type anorthosites and layered intrusions. Their geneses have long been controversial, with existing hypotheses including liquid immiscibility between Si-rich and Fe–Ti–P-rich melts and gravitational fractionation among apatite, magnetite, ilmenite and silicates. In this paper, we report detailed field geology and mineral geochemical studies of the nelsonite and Fe–Ti oxides ore from the Damiao anorthosite complex, NE China. Geological observations indicate that the nelsonite and Fe–Ti oxides ore occur as irregularly inclined stratiform-like or lensoid or veins, and are in sharp contact with the anorthosite and gabbronorite. The widespread veins and lenses structure of the Damiao nelsonite and Fe–Ti oxides ore in the anorthosite indicates their immiscibility-derived origin. The apatite in the nelsonite and gabbronorite shows evolution trends different from that in the gabbronorite in the diagrams of Sr versus REEs and Eu/Eu*, suggesting that petrogenesis of the nelsonite and gabbronorite is different from the gabbronorite. Compared with the gabbronorite, the nelsonite and Fe–Ti oxides ore have magnetite high in Cr, plagioclase high in Sr and low in An, and apatite high in Sr, low in REEs with negative Eu anomaly. The evidence permits us to propose that the Damiao Fe–Ti oxides ore/nelsonite and gabbronorite were derived from different parental magmas. The gabbronorite was formed by solidification of the interstitial ferrodioritic magma in the anorthosite, which was the residual magma after extensive plagioclase and pyroxene crystallization and was carried upward by the plagioclase crystal mesh. In contrast, the Fe–Ti oxides ore and nelsonites and mangerite were produced by crystallization of the Fe–Ti–P-rich and SiO_2-rich magmas, respectively, due to the liquid immiscibility that occurred when the highly evolved ferrodioritic magma mixed with newly replenished magmas. The variation from Fe–Ti oxides ore to nelsonite and gabbro-nelsonite upwards (as apatite content increases with height) in the steeply inclined Fe–Ti oxides orebodies suggest that gravity fractionation may have played important roles during the crystallization of the Fe–Ti–P-rich magma.

© 2016 Elsevier B.V. All rights reserved.

1. Introduction

Nelsonite comprises mainly magnetite, ilmenite and apatite, and is commonly present in Proterozoic massif-type anorthosites (Ashwal, 1993; Charlier et al., 2015; Chen et al., 2013; Duchesne, 1999; Dymek and Owens, 2001; Owens and Dymek, 1992; Watson and Taber, 1910) and minor in layered intrusions (Charlier et al., 2005, 2008; Tollari et al., 2008; Vantongeren and Mathez, 2012; Von Gruenewaldt, 1993). Anorthosite-related nelsonite occurs mainly as veins and lensoidal intrusions in anorthosite complex or wall rocks, e.g., the St. Urbain- and Labrieville massifs in Canada (Dymek, 1997; Dymek and Owens, 2001; Morin, 1969). Early research on nelsonite, based on its morphology, its contact relationship with wall rocks and its Fe–Ti oxides: apatite ratio (2:1), suggested that nelsonite is formed by the cooling of an Fe–Ti–P-rich magma injecting into the fractures of plutons (Kolker, 1982; Reynolds, 1985; Watson and Taber, 1913). An experimental study by Philpotts (1967) reveals that under 1400 °C, dioritic magmas can generate Fe–Ti–P-rich magma via liquid immiscibility, with the resulting nelsonite containing an oxide: apatite ratio of ca. 2:1. Lindsley (2003) argued that dioritic magmas in the nature can hardly reach 1400 °C, and recent studies suggest that segregation of a Fe-rich- and a Si-rich magma can occur at around 950 °C — 1200 °C during late fractionation of basaltic magmas (Charlier and Grove, 2012; Schmidt et al., 2006;

* Corresponding author at: State Key Laboratory of Ore Deposit Geochemistry, Institute of Geochemistry, Chinese Academy of Sciences, 99 Lincheng West Road, Guanshanhu District, Guiyang 550081, PR China.
E-mail address: songxieyan@vip.gyig.ac.cn (X.-Y. Song).

http://dx.doi.org/10.1016/j.oregeorev.2016.05.028
0169-1368/© 2016 Elsevier B.V. All rights reserved.

Veksler et al., 2006, 2007). However, the Fe-rich magma formed by this segregation is not a Fe–Ti–P magma, but a SiO_2-undersaturated Fe–Ti–P-rich magma. The Fe-rich magma is enriched in Ca, Mg, Sr, REEs, Nb, Ta, Zr and Hf, whereas the Si-rich magma is enriched in Cs, Rb, K, Na and Al (Lester et al., 2013; Schmidt et al., 2006; Veksler et al., 2006).

Nevertheless, it is still controversial whether liquid immiscibility plays a dominant role in generating nelsonite and Fe–Ti oxides ore (Charlier et al., 2011; Duchesne and Liégeois, 2015; Pang et al., 2008, 2009; Song et al., 2013; Tollari et al., 2008; Vantongeren and Mathez, 2012; Zhou, 2005). This is because many liquid immiscible features appear to occur after substantial Fe–Ti oxides crystallization. For instance, Jakobsen et al. (2005) had reported Si-rich- and Fe-rich melt inclusions among the aggregated apatite in the upper part (above the Fe–Ti oxides layer) of the Skaergaard intrusion (Hunter and Sparks, 1987, 1990; Toplis and Carroll, 1995). In the lower part of the Panzhihua intrusion (Sichuan, SW China), there is no apatite in the Fe–Ti oxides ore layer, whilst in the upper part of the intrusion Fe–Ti oxides content accounts for <10% of the apatite-bearing gabbros (Song et al., 2013), and Si-rich and Fe-rich melt inclusions were found in the apatite (Wang et al., 2013). Therefore, it is important to elucidate whether the evolution of a mantle-derived magma can lead to the segregation of a Si-rich and a Fe-rich phase, and whether this segregation can only happen at the late fractionation stage.

This study focuses on the formation of the nelsonite and Fe–Ti oxide ore in the Damiao anorthosite complex in eastern China on the bases of investigation of spatial–lithological distribution, field geology, mineral assemblage as well as whole-rock and mineral geochemistry. We analyze and compare the major- and trace element geochemistry of the Fe–Ti oxides, clinopyroxene, apatite and plagioclase to reveal their parental magma evolution and determine the timing of the immiscibility. The new data indicate that the Damiao Fe–Ti oxides ore and nelsonite have had different parental magmas from the gabbronorite, and the parental magmas of the Fe–Ti oxide ores and nelsonite were less fractionated than that of the gabbronorite. Liquid immiscibility may have been related to the mixing between a residual magma and a new primitive magma replenishment. The immiscibility may have formed a Fe–Ti–P-rich magma, which fractionated magnetite, ilmenite and apatite, and subsequently formed nelsonite and Fe–Ti oxides ore via gravitational differentiation. Late fractionation of this residual magma may have crystallized anhedral plagioclase and clinopyroxene, thus forming gabbro-nelsonite.

2. Geological Background

The North China Craton is divisible into two Archean to Paleoproterozoic blocks, called the Eastern- and Western Blocks, separated by the Paleoproterozoic Trans-North China Orogen (Fig. 1; Zhao et al., 2000, 2002). The Eastern Block consists predominantly of ca. 2.7–2.5 Ga TTG gneisses and minor supracrustal rocks (ca. 2.8–2.5 Ga), with some Early to Middle Archean rocks exposed locally. The basement of the Western Block has structural styles and metamorphic history essentially similar to those of the Eastern Block, but differs in the absence of Early to Middle Archean rocks. The Eastern- and a Western Blocks assembled at ca. 1.85 Ga to form the cratonic basement (Zhao et al., 2000). The Damiao anorthosite complex is located in the northern part of the

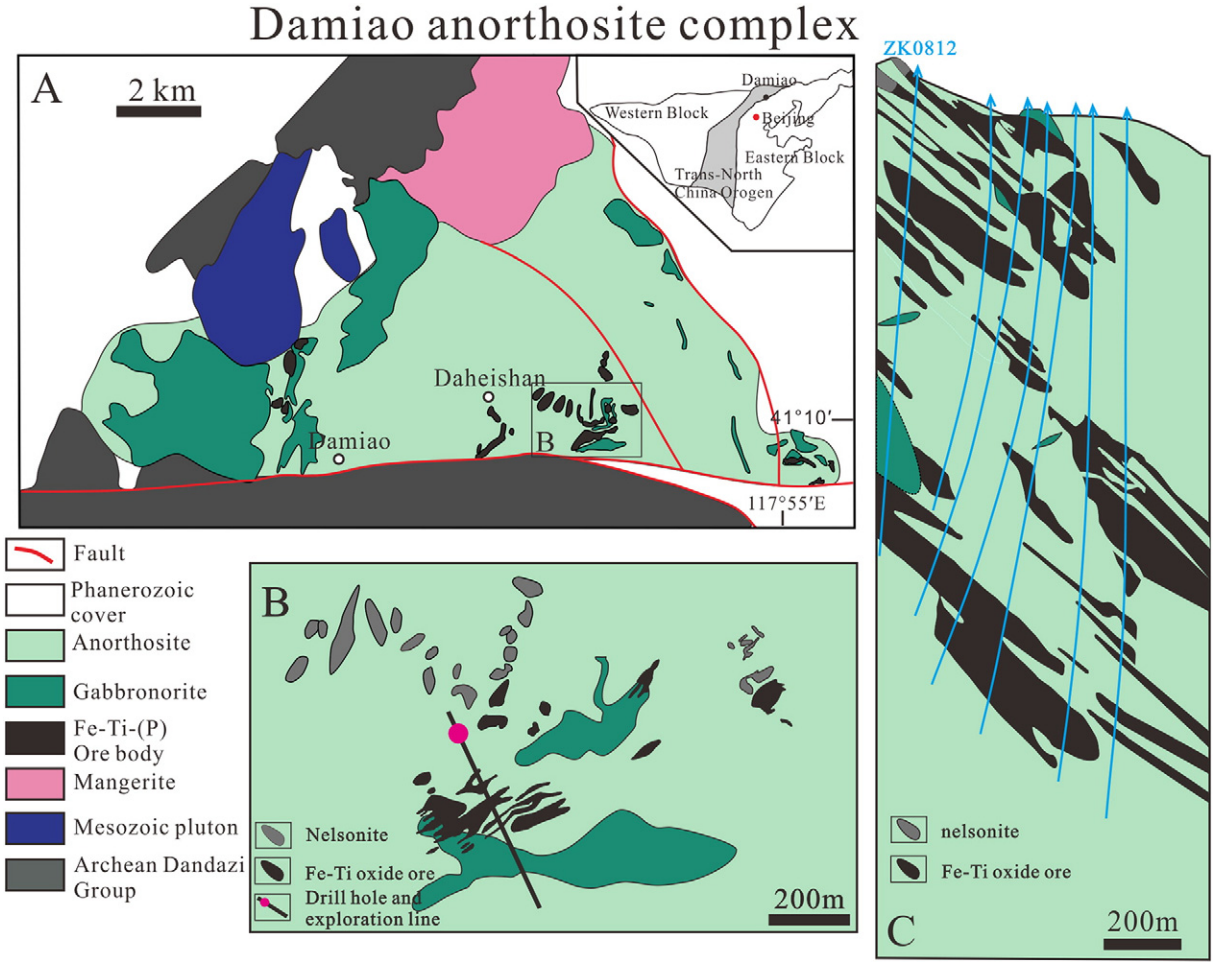

Fig. 1. A. Geologic map of the Damiao anorthosite complex; B. Lensoidal, irregularly-shaped veins of nelsonite and Fe–Ti oxides ore intruded into the anorthosite and gabbronorite; C. Cross section of the exploration line. Orebodies are lensoid or stratiform-like and situated (in the topographic lows) in the southern part of the anorthosite intrusion with various orientations, and wall rocks are anorthosite and gabbronorite (modified from the #4 Brigade of the Hebei BGMR, 2009).

Trans-North China orogenic belt (Fig. 1A). It has an outcrop area of >120 km^2 and was emplaced into the Archean Dandazi Group amphibole-plagioclase gneiss (Fig. 1A), which constitutes the most important part of a regional Anorthosite–Mangerite–Charnockite–Rapakivi–Granites (AMCG) suite (ca. 1680–1740 Ma) (Yang et al., 2005; Zhang et al., 2007; Zhao et al., 2009). Zircon U–Pb dating indicated that the Damiao anorthosite was formed at 1727 ± 9 Ma (Zhang et al., 2007).

Zhang et al. (2007) suggested that primary magma of the Damiao anorthosite was produced by basaltic magma derived from the partial melting of the EM-I mantle with some assimilation of lower crustal materials. Alternatively, Zhao et al. (2009) argued that primitive magma of the Damiao anorthosite was formed by 75% partial melting of the lower crustal rocks that were dragged into the mantle during the ca. 1.85 Ga East- and West-Blocks collision.

3. Petrology of the anorthosite complex, nelsonite and Fe–Ti oxides orebodies

The Damiao complex comprises mainly anorthosite (~85 vol.%), gabbronorite (~10 vol.%) and mangerite (~4 vol.%) (Ye et al., 1996).

The dominating anorthosite (Fig. 1A) is mainly comprised of coarse-grained plagioclase (>1 cm long) with An content of ca. 40–50 and minor orthopyroxene megacrysts (<10 vol.%). The orthopyroxene (1–10 cm long) is characterized by exsolution of plagioclase lamellae and contains up to 9 wt.% Al_2O_3 (Xie, 2005; Zhao et al., 2009). Such high-Al orthopyroxene megacrysts were also identified in the Rogaland anorthosite complex (SW Norway) and the Nain anorthosite complex, (Canada), and were attributed to high pressure crystallization at ca. 30–35 km depths (Bybee et al., 2014; Charlier et al., 2010; Emslie, 1975; Longhi et al., 1993).

In the eastern part of the Damiao complex, the gabbronorite occurs as lenses in the anorthosite with sharp contact, and anorthosite xenoliths were found in the gabbronorite lenses (Figs. 1A, 2A). The gabbronorite consists of medium-grained plagioclase (30–60 vol.%), orthopyroxene (20–30 vol.%), clinopyroxene (10–20 vol.%) and Fe–Ti oxides (10–20 vol.%), as well as minor euhedral to subhedral apatite (Fig. 3C). Mangerite occurs only in topographic highs in the northern part of the Damiao complex (Fig. 1A). The rocks contain perthite, orthopyroxene and plagioclase phenocrysts, and a groundmass of plagioclase, K-feldspar, quartz, clinopyroxene and minor Fe–Ti oxides and apatite.

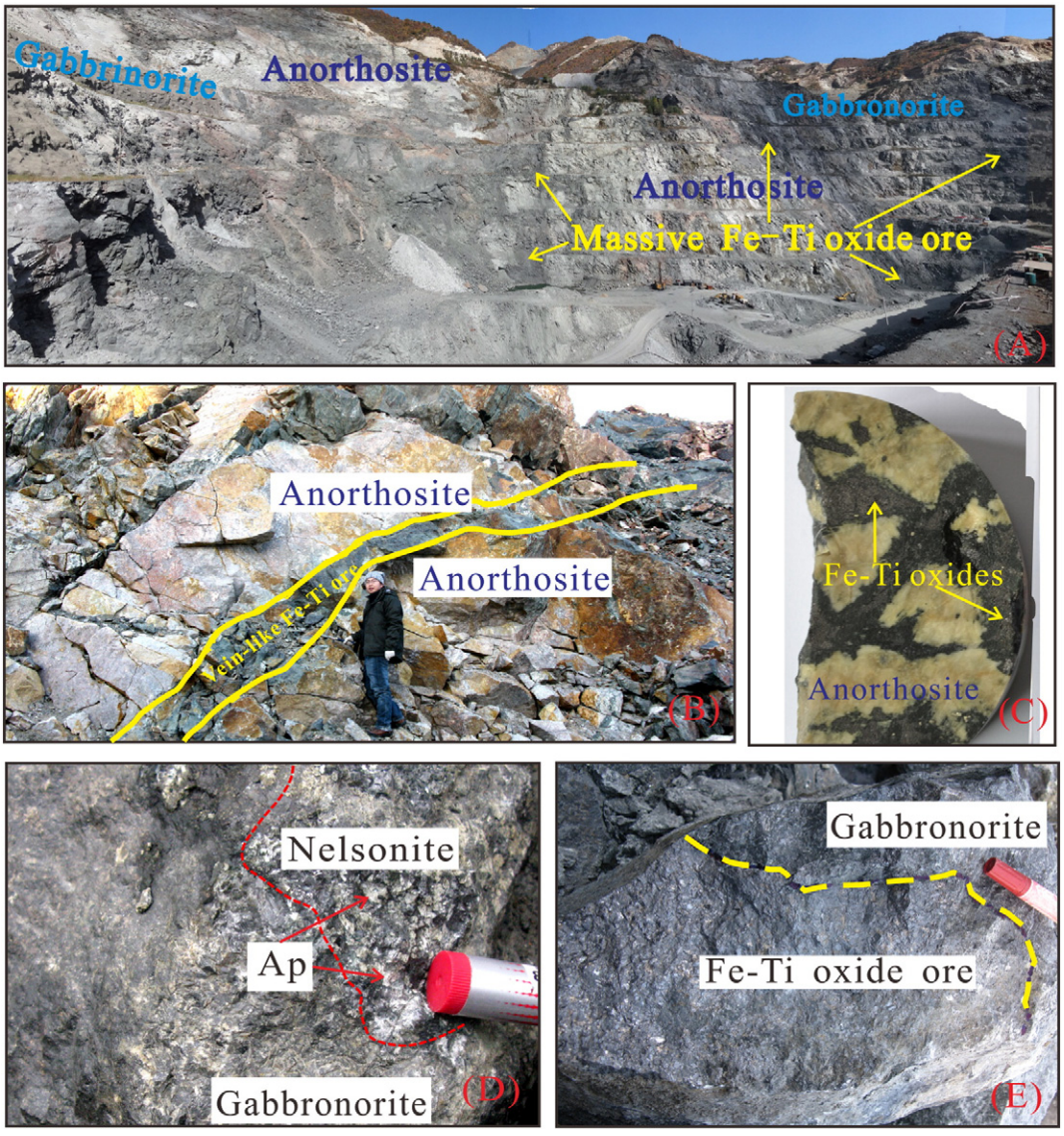

Fig. 2. Field relationship between the massive Fe–Ti ores and their host rocks. A. Field photo of the Damiao Fe–Ti–P open pit; B. Vein-like Fe–Ti oxides ore (oxides >90 vol.%)in sharp intrusive contact with the hosting anorthosite; C. "net-texture" Fe–Ti oxides ore: Coarse-grained plagioclase surrounded by oxide ores. Ore sample from the contact between anorthosite and massive Fe–Ti oxides ore; D. Sharp and irregular contact between nelsonite (apatite + oxide >90 vol.%) and gabbronorite (oxide <20 vol.%); E. Sharp and irregular contact between Fe–Ti oxides ore (oxides >90 vol.%) and gabbronorite (oxide <20 vol.%). Abbreviation: Ap: apatite.

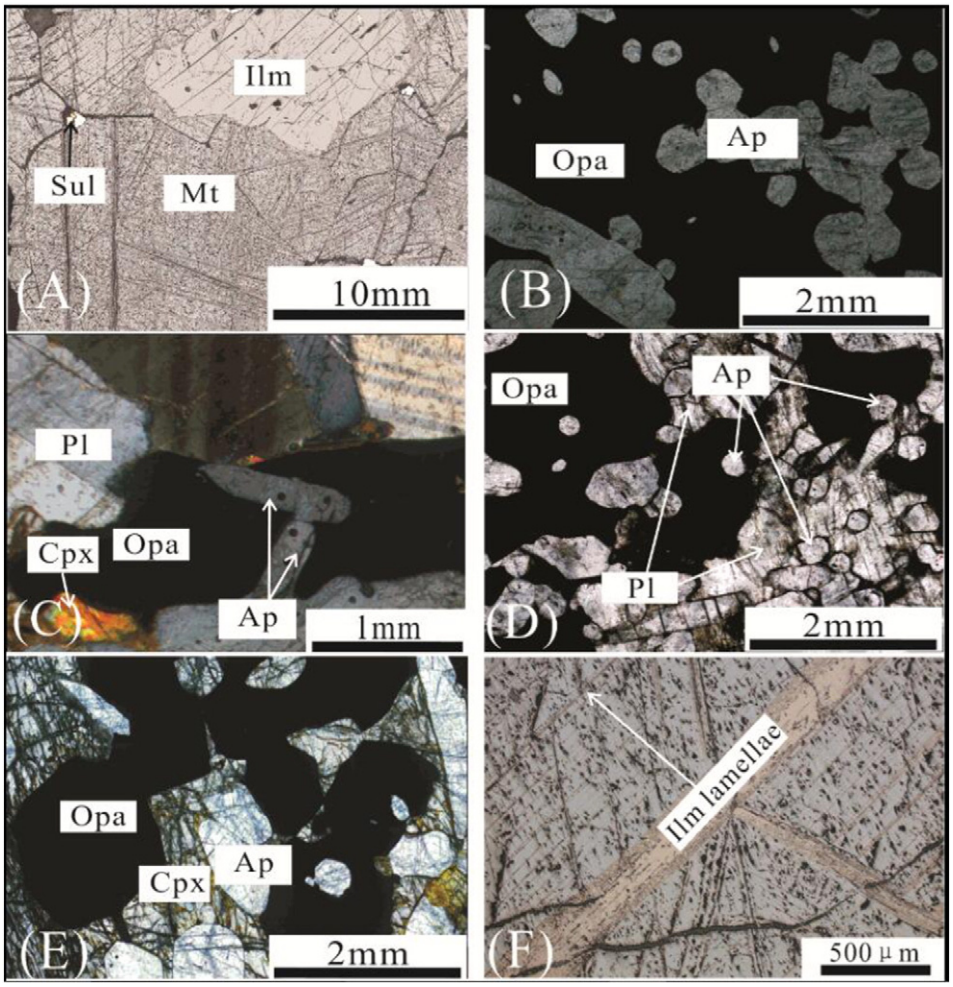

Fig. 3. photomicrographs of the Damiao rocks and ores. A. Massive Fe–Ti ore from the lower part of the anorthosite complex: Coarse-grained euhedral magnetite and ilmenite contain sharp boundary. Ilmenite exsolution lamellae on magnetite surface, whereas ilmenite surface is smooth and has no exsolution texture. Reflected light; B. Nelsonite from the middle part of the anorthosite complex: Euhedral magnetite, ilmenite and euhedral to subhedral apatite accounting for up to 90% of the rock. Crossed polar; C. Plagioclase, oxides and euhedral to subhedral apatite in gabbronorite. Crossed polar; D. Gabbro-nelsonite from the top of the anorthosite complex: Interstitial anhedral plagioclase among Fe–Ti oxides and euhedral to subhedral apatite. Crossed polar; E. Gabbro-nelsonite: Interstitial anhedral clinopyroxene among Fe–Ti oxides and apatite. Crossed polar; F. Ilmenite exsolution lamellae from magnetite. Lamellae thickness: 10 μm — 100 μm. Abbreviations: Ilm: ilmenite; Mt.: magnetite; Ap: apatite; Pl: plagioclase; Cpx: clinopyroxene; Opa: opaque oxides.

In general, Fe–Ti oxides orebodies are lensoid or steeply inclined stratiform-like, and are situated (in the topographic lows) in the southern part of the anorthosite intrusion with various orientations (Fig. 1). It is remarkable that the lensoid or stratiform-like orebodies show irregular shape in exploration line cross section (Fig. 1C) and undirectional in the geological map (Fig. 1B). These orebodies are in sharp contact with the anorthosite (Figs. 2A, B). The Fe–Ti oxides ore veins locally crosscut the gabbronorite with sharp and irregular contact at the boundary of large Fe–Ti oxides lenticular orebody (Fig. 2D, E). Along the contact between the Fe–Ti oxides ore and the anorthosite/gabbronorite, coarse-grained pyroxene and plagioclase are surrounded and crosscut by thin and undirectional Fe–Ti oxides veins, forming local "net-texture" ore (Fig. 2C). With the increase of apatite content, Fe–Ti oxides ore grades into nelsonite (Chen et al., 2013). Therefore nelsonite is seldom found in drill cores but outcrops extensively in topographic highs (Fig. 1B).

The Fe–Ti oxides ore comprises mainly coarse-grained (5–10 mm) magnetite (70–90 vol.%) and ilmenite (8–15 vol.%), with normally <1 vol.% apatite (Fig. 3A). Nelsonite generally comprises densely disseminated or semi-massive coarse-grained euhedral to subhedral magnetite and ilmenite, as well as rounded or tabular apatite (20–60 vol.%). Boundaries between titanomagnetite and ilmenite grains are sharp (Fig. 3B). These petrographic features resemble the nelsonite from the St. Urbain- and Labrieville massifs in Canada (Dymek and Owens, 2001). It is noteworthy that the nelsonite occurs in the upper part of the Damiao complex and comprises the upper portions of the Fe–Ti oxide orebodies, and gabbro-nelsonite occur above the nelsonite and consists of euhedral magnetite, ilmenite, apatite and (up to 20 vol.%) interstitial anhedral clinopyroxene and plagioclase (Fig. 3D, E). In this paper, we define the nelsonite containing 10–20 vol.% silicates as gabbro-nelsonite. No exsolution texture occurs in ilmenite (Fig. 3A), whereas ilmenite exsolution lamellae (<10 vol.%; 1–100 μm wide) and spinel (< 10 μm long) occur along the magnetite (100) and (111) crystal planes (Fig. 3F).

The gabbroic- and ferrodioritic dykes occur mainly along the margins of the complex, where they intruded the anorthosite. High-Al gabbroic dykes are considered to be parental to the associated anorthosite, and the ferrodioritic dykes may represent residual liquids remained after substantial plagioclase and orthopyroxene crystallization (Zhao et al., 2009).

4. Sampling and analytical methods

In this study, 13 samples of nelsonites and gabbro-nelsonites were collected from mountain tops of the Damiao complex, and 35 samples of Fe–Ti oxides ores were collected from the Drill Hole ZK0812 (at Heishan), which intercepts the inclined Fe–Ti oxides orebody from 1300 m deep to the surface.

For whole-rock major- and trace element geochemical analyses, representative fresh rock samples were jaw-crushed and agate-milled to

200 mesh. To ensure the analyzed minerals are magmatic, we chose unaltered magnetite, ilmenite and plagioclase, granular clinopyroxene and euhedral apatite for the electron microprobe (EMPA) and LA–ICP–MS analyses. In addition, we have analyzed the exsolved ilmenite lamellae to determine whether the euhedral ilmenite was also formed as external granule exsolution.

Major element geochemistry was analyzed by X-ray Fluorescence Spectrometer (XRF) at the ALS Laboratory Group, whereas trace element geochemistry was analyzed by ICP–MS at the Institute of Geochemistry, Guiyang (Chinese Academy of Sciences) (GYIGCAS). Detailed analytical methodology was outlined in Qi et al. (2000), and the whole-rock geochemical data are listed in Appendix I.

Major element geochemistry of magnetite, ilmenite, clinopyroxene and apatite were analyzed by electron microprobe (EMPA-1600) at the GIGCAS. Analytical conditions: Electron beam diameter: 10 μm; Accelerating voltage: 25 kV; Electron beam current: 10 nA. EMPA results are listed in Appendix II.

Trace element geochemistry of apatite, plagioclase, magnetite and ilmenite were analyzed by LA–ICP–MS at the GYIGCAS, using the GeoLasPro laser-ablation system and Agilent 7700x. Analytical conditions: Laser beam (for apatite and plagioclase ablation): 44 μm (diameter) and 6 Hz (frequency); Standards: NIST610, BCR-2G, BIR-1G and BHVO-2G. The detailed analytical and data processing methodology were outlined in Liu et al. (2008). Laser beam (for magnetite and ilmenite ablation): 60 μm (diameter); 6 Hz (frequency). After processing the raw data with iolite, standard curve was produced and results were calculated with ^{57}Fe (internal standard) and GSE-1G (external standard). Detailed analytical and data processing methodology were listed in Dare et al. (2012) and She et al. (2015). In this study, the international standards of BIR-1G, BHVO-2G and BC-28 (massive magnetite from the Bushveld intrusion) (Dare et al., 2012) were adopted for quality control on the data analytical results. As listed in Appendix III, the analytical results of BIR-1G, BHVO-2G and BC-28 were all very close to their reference values, suggesting high accuracy of the analyses undertaken. Standard analytical values and detection limits of this study were listed in Appendix III.

5. Results

5.1. Whole-rock geochemistry

For most of the nelsonite analyzed, the total content of $CaO + FeO + Fe_2O_3 + TiO_2 + P_2O_5$ are >90 wt.%, consistent with the (optical microscopy) petrographic observation that nelsonite comprises mainly apatite, magnetite and ilmenite (Fig. 3A, B). Phosphate (P_2O_5) content ranges 8.0 to 17.2 wt.%, consistent with the wide range of apatite content in nelsonite, and with the variable (non-2:1) Fe–Ti oxides/apatite ratio. Fig. 4 shows that gabbro-nelsonite contains 10–40 wt.% SiO_2, coinciding with anhedral silicates reaching 20 vol.%. Fig. 5A shows that Rare Earth Elements (REEs) and P_2O_5 are positively correlated, and that the nelsonite contains the highest REEs content, which suggest that apatite is the major sink for REEs. Anorthosite contains the highest Sr and Al_2O_3 contents, and Sr and Al_2O_3 are also positively correlated (Fig. 5B), suggesting plagioclase is the major host for Sr. Both nelsonite and gabbro-nelsonite are high in Sr, indicating that Sr is compatible to both plagioclase and apatite (Duchesne, 1978; Okamoto, 1979; Prowatke and Klemme, 2006). It is noteworthy that no distinct Eu anomaly occurs in the nelsonite or gabbro-nelsonite (Fig. 6B, C), whereas distinct positive Eu anomaly is present in the gabbronorite ($Eu/Eu^* = 1.70–2.8$). Besides, the nelsonite and gabbro-nelsonite contain higher REEs contents than the gabbronorite (Fig. 6).

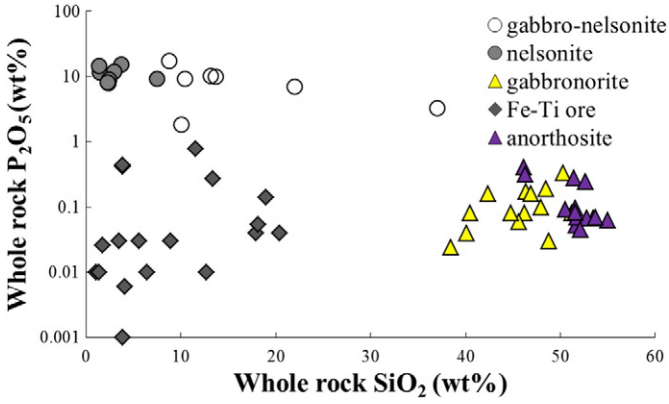

Fig. 4. SiO_2 vs P_2O_5 variation diagram of the various Damiao rock types.

5.2. Oxides and exsolved ilmenite

Tables 1 and 2 show the trace element characteristics of the Damiao magnetite and ilmenite. The Damiao magnetite is enriched in Mg, Ti, V, Cr, Mn, Co, Ni and Ga, similar to the anorthosite-related magnetite reported by Dare et al. (2014). Apart from Mg, Sc, V, Cr and Mn, the Damiao ilmenite is also enriched in High Field Strength Elements (HFSEs) such as Nb, Ta, Zr and Hf, consistent with the Skaergaard ilmenite reported by Jang and Naslund (2003). For the same samples, geochemistry of the exsolved ilmenite lamellae and euhedral ilmente are markedly different (Table 3). Elements that are of ilmenite affinity, such as Nb, Ta, Zr, Hf and Sc are lower in the exsolved ilmenite lamellae than in euhedral one, whereas elements that are of magnetite affinity, such as Ni, Cr, Co and Ga are higher in the exsolved ilmenite. This suggests that the euhedral and subhedral ilmenite were primary and not formed by external granule exsolution.

We have used mass balance calculation to estimate the influence of exsolution on magnetite composition. The formula is $F_i = A_i/(A_i + B_i)*100\%$ ($A_i = C^i_{Ilm}*X$; $B_i = C^i_{Mt}*(1-X)$), with X being the proportion of the ilmenite exsolved from magnetite, and A_i and B_i representing the amount of element "i" in the exsolved ilmenite and resulting magnetite, respectively. C^i_{Ilm} and C^i_{Mt} are the measured values of the element "i" in the ilmenite lamellae and magnetite, respectively. Since it is hard to determine the ratio of the ilmenite exsolved from magnetite (X) accurately, the ilmenite exsolution was assumed to have reached 10 modal % (petrographic observation indicates that the proportion of ilmenite lamellae in the Damiao magnetite is always below 10 modal %). Our calculation indicates that the variation of V, Cr, Ni and Ga contents in the original magnetite is below 5%, suggesting that even in the magnetite (with the most ilmenite lamellae), influence of ilmenite exsolution on the Cr, V, Ni and Ga contents in magnetite is insignificant. Besides, exsolution is absent in the Damiao euhedral ilmenite, i.e., no sub-liquidus exsolution influence. Furthermore, Cr is positively correlated with Ni in the magnetite and ilmenite (Fig. 7), suggesting that there is an equilibrium relationship between the two minerals.

5.3. Apatite and other minerals

All the apatite analyzed are high-F, magmatic apatite, with $F/Cl >> 1$ and F > 1% (Appendix II). Apatite from the Damiao nelsonite and gabbro-nelsonite contains similar REE patterns (Table 4), and the apatite from the Damiao gabbronorite contains higher LREEs (Fig. 6A) and distinct negative Eu anomaly ($Eu/Eu^* = 0.23–0.52$). On the contrary, apatite from the nelsonite and gabbro-nelsonite contains weak negative Eu anomaly ($Eu/Eu^* = 0.62–0.91$) (Fig. 8B). Besides, in the total REEs vs. Sr diagram (Fig. 8A), apatite from the nelsonite and gabbro-nelsonite contains positively correlated total REEs and Sr, whereas that for the apatite from gabbronorite is negatively correlated. Apatite from the nelsonite and gabbro-nelsonite contains lower total REEs (1400–2570 ppm) and higher Sr (520–1100 ppm); whereas apatite from the gabbronorite contains higher total REEs (2200–3500 ppm) and lower Sr (500–600 ppm).

Fig. 9A shows that the Damiao gabbronorite contains positively correlated plagioclase An and clinopyroxene Mg# contents. Plagioclase

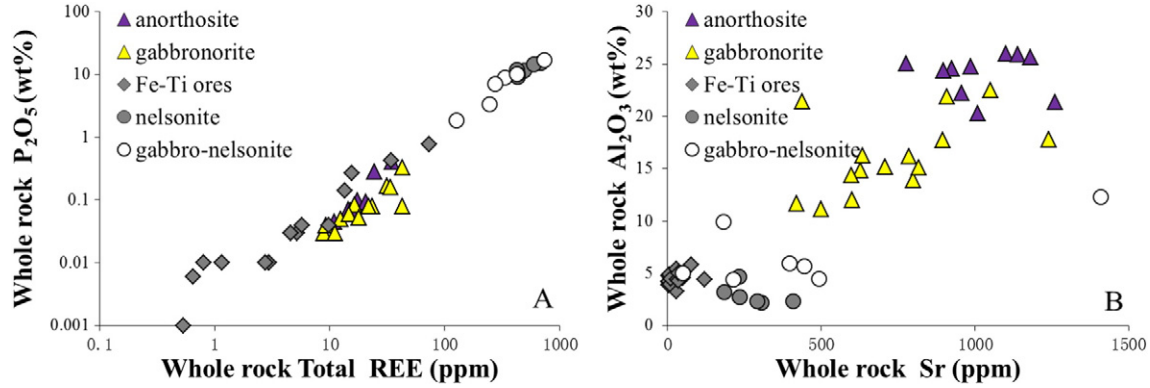

Fig. 5. A. Positive correlation between the whole-rock REEs and P_2O_5, with nelsonite containing the highest REEs; B. Positive correlation between the whole-rock Sr and Al_2O_3, with the anorthosite containing the highest Sr.

from the gabbronorite contains positively correlated An and Sr contents (Fig. 9B), similar to the plagioclase from the Rogaland anorthosite complex (Charlier et al., 2006; Duchesne, 1978). Plagioclase from the gabbro-nelsonite contains relatively high Sr but low An. Positive correlation is present in the Sr content in the plagioclase and apatite (from the gabbronorite and gabbro-nelsonite), and both plagioclase and apatite from the Damiao gabbronorite contain lower Sr than their Damiao gabbro-nelsonite counterparts (Fig. 10A).

The mineral geochemical difference between gabbronorite and nelsonite/gabbro-nelsonite is also reflected in their apatite and Fe–Ti oxides. Strontium correlates positively with Mg in the apatite from both the nelsonite and gabbro-nelsonite (Fig. 10B), and apatite from the gabbronorite contains lower Sr and Mg contents. Besides, magnetite from the nelsonite and Fe–Ti oxides ore contains higher and wider range of Cr (1118–4814 ppm, except for HB2–34Mt; average: 2462 ppm) than that from gabbronorite (1000–2100 ppm; average: 1726 ppm) (Fig. 10D). Ilmenite from the nelsonite and Fe–Ti oxides ore contains high Mg and low Mn, in complete contrast with that in the gabbronorite (Fig. 10C).

5.4. Calculated composition of parental magma

A calculation of the composition of the magmas from which the apatite crystallized may be obtained by inversion of these element concentrations using the equation: $C_l = C_{ap}/D$. Where C_1 = concentration of the element in the liquid, C_{ap} = concentration of the element in apatite and D = partition coefficient (Table 5). Fig. 11 shows the chondrite-normalized trace element patterns for parental magmas of the various Damiao rock types. The partition coefficients used for this calculation were from Bedard (2001). As shown in Fig. 11, the calculated composition of the magma in equilibrium with the apatite in the gabbronorite contains negative Sr and Eu anomalies, similar to the ferrodioritic dykes (Zhao et al., 2009). Besides, calculated parental magmas in equilibrium with the apatite in the nelsonite and gabbro-nelsonite contain

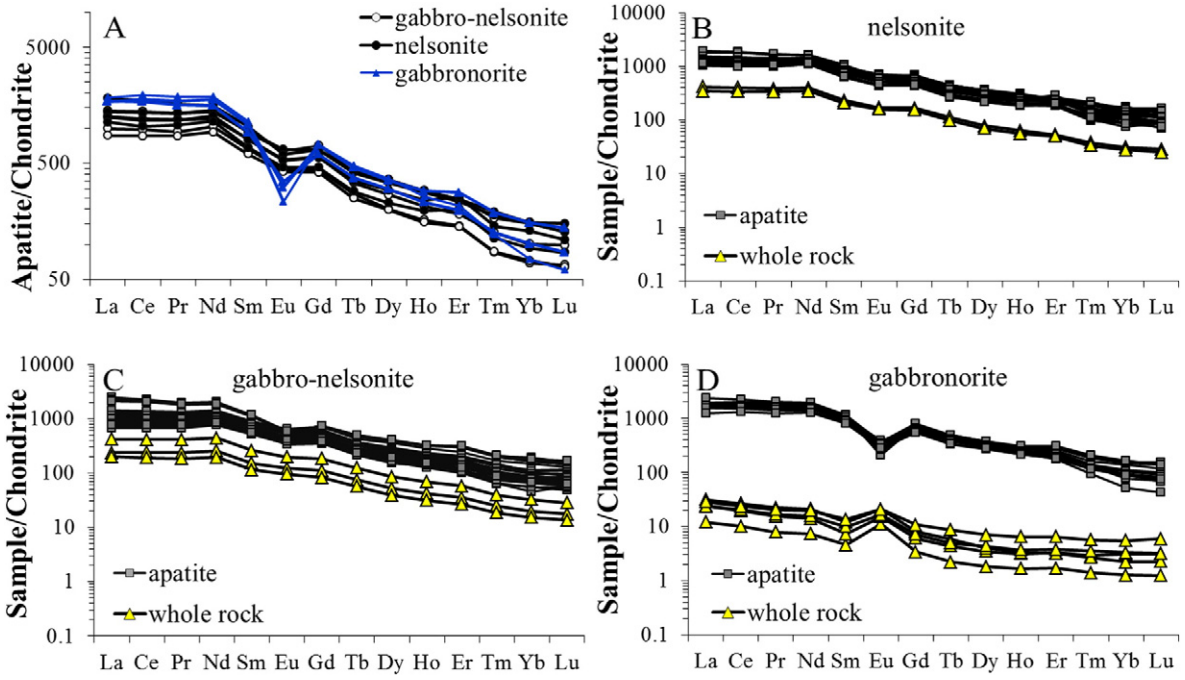

Fig. 6. A. Apatite from the gabbronorite contains distinct negative Eu anomaly and high REEs, whereas negative Eu anomaly in apatite from the nelsonite and gabbro-nelsonite is indistinct; B. Apatite from the nelsonite does not have distinct Eu anomaly. Similar REE patterns present for the whole rock and apatite, suggesting REE content mainly controlled by apatite; C. Apatite from the gabbro-nelsonite does not have distinct Eu anomaly, and its REE pattern is similar to that in the whole rock; D. Apatite from the gabbronorite contains distinct negative Eu anomaly. Chondrite values are from Sun and McDonough (1989).

Table 1
Representative trace element geochemistry of magnetite.

		ZK12-93MT	ZK12-87MT	ZK12-88MT	ZK12-90MT	ZK12-82MT	ZK12-33MT	ZK12–66MT	ZK12–78MT	ZK12–73MT
		Gabbronorite	Gabbronorite	Gabbronorite	Gabbronorite	Gabbronorite	Gabbronorite	Fe–Ti ores	Fe–Ti ores	Fe–Ti ores
Mg	LA-ICPMS	520.83	434.06	3161.20	1239.23	2514.67	171.51	4796.83	4695.20	4862.67
Sc	LA-ICPMS	1.98	3.30	6.42	7.07	5.10	1.65	2.58	6.77	1.51
Ti	LA-ICPMS	1938.57	33,092.30	22,175.33	28,065.67	18,971.50	1441.33	16,939.20	37,274.33	5372.73
V	LA-ICPMS	4716.83	4501.70	5006.63	4611.97	4674.80	4622.23	4424.33	4275.73	4796.60
Cr	LA-ICPMS	1950.73	1927.30	2096.77	2132.73	996.63	1253.87	2535.17	2699.77	2519.90
Mn	LA-ICPMS	328.56	1662.38	641.47	1597.33	750.56	127.35	579.44	1105.13	318.67
Co	LA-ICPMS	44.25	49.68	143.57	168.90	60.41	44.76	93.34	117.36	125.38
Ni	LA-ICPMS	94.80	113.26	167.01	250.27	96.52	233.98	114.69	241.83	241.93
Cu	LA-ICPMS	0.09	0.11	2.00	0.04	1.23	5.73	2.25	0.25	0.00
Zn	LA-ICPMS	1980.97	1218.15	792.08	716.91	280.71	100.12	760.84	393.37	504.88
Ga	LA-ICPMS	54.38	44.50	72.72	72.33	54.09	35.16	40.99	58.77	36.09
Zr	LA-ICPMS	0.84	0.97	1.02	4.53	2.68	0.23	2.09	3.05	1.64
Nb	LA-ICPMS	0.12	0.03	0.08	0.36	0.08	0.14	0.00	0.02	0.00
Hf	LA-ICPMS	0.08	0.08	0.06	0.13	0.06	0.04	0.05	0.10	0.03
Ta	LA-ICPMS	0.03	0.00	0.01	0.06	0.01	0.12	0.00	0.00	0.00

Table 1 (*continued*)

	HB2-33MT	HB2-7MT	HB2–20MT	ZK12-44MT	ZK12–23MT	ZK12–28MT	HB2-16MT	ZK12-46MT	HB12–6MT	HB12-8MT
	Fe–Ti ores	Fe–Ti ores	Fe–Ti ores	Fe–Ti ores	Fe–Ti ores	Fe–Ti ores	Nelsonite	Nelsonite	Nelsonite	Nelsonite
Mg	5525.17	2703.40	2720.73	1089.88	408.68	193.05	680.86	328.60	788.17	1168.00
Sc	7.53	4.17	0.83	4.63	0.93	3.29	1.45	3.17	3.96	2.32
Ti	30,068.00	23,091.80	6056.43	11,728.35	6977.20	16,423.80	6424.63	9798.00	12,314.30	2715.90
V	3379.60	4744.39	4331.53	4581.98	4645.36	4769.24	4416.35	4325.30	4632.12	4871.53
Cr	1891.21	1675.66	1915.27	1807.00	4701.30	1899.90	1118.31	3407.10	3212.90	3695.70
Mn	1127.09	753.69	302.21	434.85	286.36	501.77	350.47	543.03	402.76	202.76
Co	75.43	62.14	112.60	78.73	97.85	62.00	71.97	80.01	64.86	63.15
Ni	81.33	104.81	142.77	88.97	191.48	225.57	96.03	93.46	91.34	96.11
Cu	0.15	0.00	0.84	8.12	1.40	0.47	4.55	5.83	0.42	1.40
Zn	452.86	252.90	487.81	2600.93	2773.07	9216.33	1410.38	7815.43	219.55	89.08
Ga	61.71	59.06	59.75	86.92	142.48	124.07	80.88	66.24	59.66	57.78
Zr	5.49	2.34	1.71	1.96	1.52	2.56	1.53	0.78	2.06	0.76
Nb	0.09	0.01	0.00	0.00	0.01	0.04	2.07	0.92	0.00	0.25
Hf	0.12	0.10	0.04	0.06	0.04	0.10	0.29	0.10	0.07	0.06
Ta	0.03	0.00	0.00	0.01	0.00	0.00	0.97	0.18	0.00	0.10

Table 2
Representative trace element geochemistry of ilmenite.

		ZK12-93ILM-3	ZK12-87ILM	ZK12-88ILM	ZK12-90ILM	ZK12-82ILM	ZK12-33ILM	ZK12-86ILM	ZK12–66ILM	ZK12–78ILM	ZK12–73ILM	HB2-33ILM	HB2-7ILM	HB2–20ILM
		Gabbronorite	Gabbronorite	Gabbronorite	Gabbronorite	Gabbronorite	Gabbronorite	Gabbronorite	Fe–Ti ores	Fe–Ti ores	Fe–Ti ores	Fe–Ti ores	Fe–Ti ores	Fe–Ti ores
Mg	LA-ICPMS	455.82	720.38	4564.60	1127.56	4014.70	444.74	291.28	7830.19	9384.40	10,896.65	9235.34	5547.89	2768.19
Sc	LA-ICPMS	53.26	50.40	67.45	74.53	51.93	17.91	36.83	59.10	53.60	47.80	66.25	62.97	54.55
Ti	LA-ICPMS													
V	LA-ICPMS	532.63	465.70	626.03	546.97	344.79	623.70	459.94	438.92	381.16	640.68	355.33	538.19	352.56
Cr	LA-ICPMS	182.60	80.52	139.90	175.60	72.99	332.27	116.95	209.29	165.01	347.63	106.30	111.12	165.94
Mn	LA-ICPMS	12,854.25	11,700.25	4858.60	11,457.75	8361.23	8708.75	6641.63	6590.50	6253.28	7480.25	7233.03	5862.98	5930.55
Co	LA-ICPMS	16.14	23.55	48.15	56.41	15.24	39.86	17.54	33.41	52.51	51.58	37.27	24.53	43.30
Ni	LA-ICPMS	14.50	14.30	20.83	19.22	13.95	33.74	14.43	8.40	27.75	25.26	6.83	7.41	12.11
Cu	LA-ICPMS	6.19	11.54	7.78	11.24	11.70	18.92	11.64	6.67	8.29	2.96	5.04	6.50	2.55
Zn	LA-ICPMS	192.37	110.03	38.48	41.85	9.27	501.97	169.61	100.01	18.82	126.00	91.98	17.48	70.40
Ga	LA-ICPMS	4.47	0.36	1.99	3.81	0.30	1.89	0.69	1.42	1.05	4.10	2.14	0.33	0.97
Zr	LA-ICPMS	785.22	121.97	49.47	239.53	24.93	214.30	236.42	248.53	72.49	10.24	333.36	149.87	278.96
Nb	LA-ICPMS	70.86	40.83	61.76	36.98	8.06	21.96	59.53	19.81	26.04	4.20	21.59	18.37	24.14
Hf	LA-ICPMS	16.53	5.36	2.86	7.65	1.22	4.71	5.44	3.79	1.98	0.35	6.11	3.22	4.72
Ta	LA-ICPMS	3.13	1.58	2.71	1.58	0.25	1.00	3.36	0.91	1.14	0.11	0.81	0.78	0.99

Table 2 (*continued*)

	ZK12-44ILM	ZK12–23ILM	ZK12–28ILM	HB2-16ILM	ZK12-46ILM	HB12–6ILM	HB12-8ILM	HB2–34ILM	HB2-24ILM	HB2-35ILM	HB12-7ILM	HB12–11ILM	HB2-32ILM
	Fe–Ti ores	Fe–Ti ores	Fe–Ti ores	Nelsonite	Nelsonite	Nelsonite	Nelsonite	Nelsonite	Nelsonite	Gabbro-nelsonite	Gabbro-nelsonite	Gabbro-nelsonite	Gabbro-nelsonite
Mg	1044.78	392.87	223.24	695.07	741.63	1675.27	4790.41	5457.61	549.40	3198.87	533.60	2467.84	1344.05
Sc	54.39	44.98	37.75	52.36	91.14	77.53	77.70	71.37	56.19	80.77	67.65	68.32	68.29
Ti													
V	419.36	539.52	788.38	459.20	680.07	361.05	488.70	384.32	353.95	412.47	385.54	337.57	248.44
Cr	223.50	353.40	346.27	280.00	232.97	208.70	225.13	59.62	266.11	102.62	224.67	160.17	43.53
Mn	6659.70	7746.55	7445.76	8652.00	9112.00	5180.85	5820.28	6092.03	8781.95	5569.13	5901.25	5118.20	5556.90
Co	26.37	66.61	35.74	58.80	45.36	34.22	34.67	31.16	28.23	29.42	25.20	34.40	22.20
Ni	7.77	17.56	20.19	19.04	23.42	8.51	14.85	4.94	4.20	11.55	14.71	16.85	17.10
Cu	10.30	5.57	3.04	0.00	21.12	2.71	3.52	3.15	6.29	4.98	0.00	13.64	21.05
Zn	171.28	640.47	538.15	4256.00	818.07	7.44	24.22	12.28	274.88	109.06	27.66	10.75	24.65
Ga	2.71	0.80	0.85	45.92	9.47	0.45	2.60	0.61	0.99	4.74	0.93	1.26	0.84
Zr	242.86	102.90	79.41	10.64	1239.23	1039.55	313.34	215.31	230.56	101.41	127.81	206.44	4.56
Nb	28.85	16.51	8.17	12.54	59.56	23.44	34.07	24.85	60.76	15.58	22.92	14.71	30.12
Hf	3.02	2.13	1.74	1.23	19.26	14.65	5.76	3.26	6.00	2.55	2.79	4.30	1.14
Ta	1.09	0.83	0.33	0.78	3.75	0.76	1.65	1.02	2.13	0.74	0.95	0.41	1.23

Table 3
Composition of the exsolved ilmenite and the hosting magnetite and ilmenite.

	Fe–TiFe–Ti ores	Fe–Ti ores	Fe–Ti ores	Fe–Ti ores	Fe–Ti ores	Fe–Ti ores	Fe–Ti ores	Fe–Ti ores	Fe–Ti ores	Nelsonite	Nelsonite
	HB2–20	HB2–20	HB2–20	ZK12–73	ZK12–73	ZK12–73	ZK12–78	ZK12–78	ZK12–78	HB12–6	HB12–6
	Ilmenite lamellae	Ilmenite grain	host magnetite	Ilmenite lamellae	Ilmenite grain	host magnetite	Ilmenite lamellae	Ilmenite grain	host magnetite	Ilmenite lamellae	Ilmenite grain
Mg	9062.25	2768.19	2720.73	17,089.98	10,896.65	4862.67	13,066.95	9384.40	4695.20	2521.67	1675.27
Sc	45.86	54.55	0.83	43.87	47.80	1.51	46.19	53.60	6.77	56.96	77.53
V	338.26	352.56	4331.53	648.02	640.68	4796.60	230.25	381.16	4275.73	222.47	361.05
Cr	1050.08	165.94	1915.27	821.22	347.63	2519.90	782.46	165.01	2699.77	143.71	208.70
Mn	4232.81	5930.55	302.21	4885.56	7480.25	318.67	4809.11	6253.28	1105.13	3952.50	5180.85
Co	181.02	43.30	112.60	143.19	51.58	125.38	188.12	52.51	117.36	60.63	34.22
Ni	53.65	12.11	142.77	48.19	25.26	241.93	59.65	27.75	241.83	13.86	8.51
Cu	9.13	2.55	0.84	9.51	2.96	0.00	9.56	8.29	0.25	9.80	2.71
Zn	1584.34	70.40	487.81	1005.32	126.00	504.88	1137.36	18.82	393.37	209.19	7.44
Ga	53.32	0.97	59.75	47.43	4.10	36.09	25.87	1.05	58.77	4.38	0.45
Zr	52.39	278.96	1.71	20.02	10.24	1.64	33.83	72.49	3.05	53.37	1039.55
Nb	3.87	24.14	0.00	1.75	4.20	0.00	2.89	26.04	0.02	6.99	23.44
Hf	1.73	4.72	0.04	0.78	0.35	0.03	1.37	1.98	0.10	2.47	14.65
Ta	0.11	0.99	0.00	0.10	0.11	0.00	0.09	1.14	0.00	0.19	0.76

Table 3 (*continued*)

	Nelsonite	Nelsonite	Nelsonite	Nelsonite	Gabbro-nelsonite	Gabbro-nelsonite	Gabbro-nelsonite		
	HB12–6	HB12–2-34	HB12–2-34	HB12–2-34	HB12–11	HB12–11	HB12–11		
	host magnetite	Ilmenite lamellae	Ilmenite grain	host magnetite	Ilmenite lamellae	Ilmenite grain	host magnetite	X	Average Fi
Mg	788.17	11,734.35	5457.61	2901.70	6283.23	2467.84	1150.23	10%	29%
Sc	3.96	66.05	71.37	3.24	51.74	68.32	4.12	10%	63%
V	4632.12	358.51	384.32	3541.83	290.70	337.57	4848.13	10%	1%
Cr	3212.90	300.22	59.62	686.98	645.53	160.17	3623.97	10%	2%
Mn	402.76	4687.52	6092.03	507.10	4081.50	5118.20	285.19	10%	55%
Co	64.86	140.95	31.16	73.31	132.12	34.40	76.08	10%	13%
Ni	91.34	28.81	4.94	67.20	33.09	16.85	99.98	10%	3%
Cu	0.42	8.37	3.15	0.12	9.26	13.64	5.26	10%	47%
Zn	219.55	1838.08	12.28	416.02	1187.47	10.75	201.07	10%	20%
Ga	59.66	60.95	0.61	64.02	26.33	1.26	59.63	10%	3%
Zr	2.06	31.54	215.31	1.79	34.57	206.44	1.60	10%	66%
Nb	0.00	1.53	24.85	0.00	3.77	14.71	0.13	10%	94%
Hf	0.07	1.50	3.26	0.04	1.69	4.30	0.05	10%	76%
Ta	0.00	0.04	1.02	0.00	0.16	0.41	0.00	10%	98%

X means the proportion of the ilmenite exsolved from magnetite. The value of X reaches 10 modal % is assumed.
Fi means the variation of element "i" contents in the original magnetite. Fi is below 5% suggesting minor geochemical influence on the original magnetite.

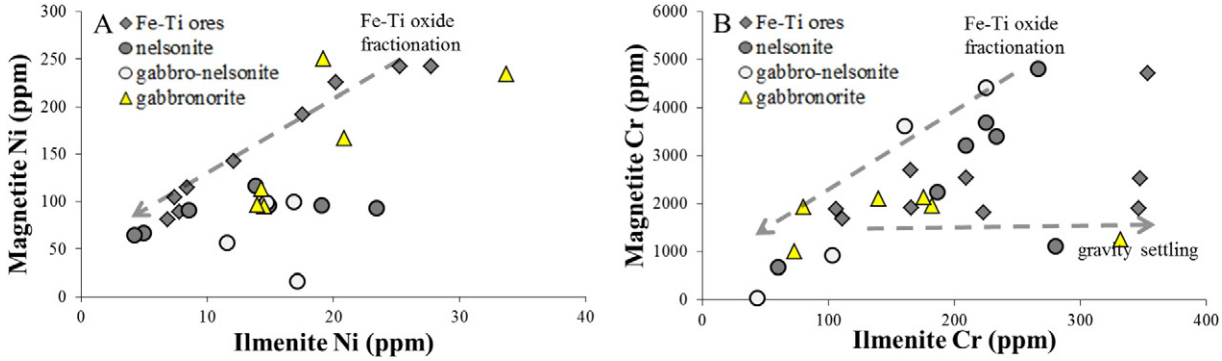

Fig. 7. Distribution of Cr and Ni in the magnetite and ilmenite.

positive Sr and Eu anomalies, and fall inside the overlapping area between the ferrodioritic dyke and high-Al gabbroic dyke.

6. Discussion

According to above description, the distinctive field geological features of the Damiao Fe–Ti oxides orebodies include: 1) the large-scale Fe–Ti orebodies are irregular steeply inclined stratiform-like or lensoid in the cross sections and undirectional on the geological map (Fig. 1), they are ca. 1–100 m thick and have sharp contact with the anorthosite; 2) the Fe–Ti orebodies comprise dominantly Fe–Ti oxides and apatite and <5 vol.% silicates; 3) the ores are coarse-grained (most magnetite and ilmenite: >5 mm in diameter); 4) the upper parts of the large orebodies comprise nelsonite and gabbro-nelsonite, as apatite and silicates contents increase with height in the Fe–Ti oxides ores. These features cannot be explained by gravitational differentiation of magnetite, ilmenite and apatite from silicates alone. The increase of apatite content upwards in the large Fe–Ti oxides orebodies and occurrence of the nelsonite in the upper part of the Damiao indicate a gravity accumulation. This suggests that the orebodies were originally steeply inclined rather than horizontal. Consistently, although the large orebodies are stratiform-like and parallel in the cross section, they are undirectional in geological map (Fig. 1). Such field relationships indicate that the nelsonite and Fe–Ti oxides orebodies were emplaced after solidification of the anorthosite and gabbronorite and cannot be explain by fractionation of a concordant magma (Fig. 2C). Experimental studies demonstrated that Fe–Ti oxides and apatite crystallize very late along with pyroxene and plagioclase during fractionation of basaltic magma (Tollari et al., 2006). Thus, the very high Fe–Ti oxides and apatite contents and the very low silicates content in the Fe–Ti oxides ores and nelsonite, as well as the coarse-grained texture can be explained by fractional crystallization of these minerals from a Fe–Ti–P-rich magma. Therefore, we agree with the liquid immiscibility hypothesis proposed by Chen et al. (2013), which suggests that the residual magma (after the anorthosite and gabbronorite formation) may form a Fe–Ti–P magma (SiO_2 < 2%) and a SiO_2-rich magma via liquid immiscibility under high oxygen fugacity. Subsequently, the Fe–Ti–P magma may be fractionated to form nelsonite and Fe–Ti oxides ore. Under low oxygen fugacity, however, the residual magma may be solidified to oxide-apatite gabbronorite. Although this late liquid immiscibility hypothesis can explain the sharp contact between the Damiao Fe–Ti oxides ore/nelsonite and anorthosite/gabbronorite, it cannot explain the reason why compared with the gabbronorite, apatite from the Damiao nelsonite and Fe–Ti oxides ore contains higher Sr, lower REEs and subtle negative Eu anomaly, or the higher Sr and Cr in the anhedral plagioclase and magnetite, respectively (Figs. 8, 10).

6.1. Mineralogical evidence for more primary Fe–Ti–P-rich magma before liquid immiscibility

Previous studies indicated that both REEs and Sr tend to enter the Fe–Ti–P-rich magma and are relatively low in Si-rich magma during liquid immiscibility (Veksler et al., 2006). Strontium and Eu are compatible in plagioclase, whereas the other REEs are not (Okamoto, 1979), and thus plagioclase fractionation would lead to distinct negative Sr and Eu anomalies in the residual magma. Strontium and most REEs are compatible to apatite, and Mg in apatite is influenced by the magma Mg content (Prowatke and Klemme, 2006). The high REEs, low Sr and distinct negative Eu anomaly of the apatite from the gabbronorite (Fig. 8A, B) suggest that apatite crystallized after substantial plagioclase fractionation associating the anorthosite formation. If the liquid immiscibility (and thus the formation of the nelsonite, Fe–Ti oxides ore and mangerite) occurred after extensive plagioclase fractionation (Chen et al., 2013), apatite from the nelsonite and gabbro-nelsonite would be Sr- and Eu-depleted and REEs-enriched, whilst the plagioclase from the gabbro-nelsonite would be Sr-depleted. In contrast, the apatite from the Damiao nelsonite contains higher Sr and Eu/Eu^* and slightly lower total REEs than that from the gabbronorite (Table 4, Fig. 8) and the plagioclase from the gabbro-nelsonite is also rich in Sr (Fig. 9B). Furthermore, the parental magmas of the nelsonite and gabbro-nelsonite equilibrium with apatite contain positive Sr and Eu anomalies, and plot between the ferrodioritic dyke and high-Al gabbroic dyke (Fig. 11). These suggest that the liquid immiscibility may have occurred after mixing of a highly evolved residual magma (ferrodioritic magma) with a relatively primary magma (high-Al gabbroic magma) (Figs. 8A, 11). Such magma mixing resulted in increase in Sr, Mg and Eu and decrease in REEs and Mn in the new magma. The new magma then separated into Fe–Ti–P-rich and SiO_2-rich magmas, which formed the Fe–Ti oxide orebodies and mangerite, respectively. Thus, the apatite of the nelsonite crystallized from the Fe–Ti–P-rich magma is enriched in both Sr and Eu, and may be depleted in REEs relative to the apatite in the gabbronorite (Figs. 8, 10B). As illustrated in Fig. 8, nelsonite/gabbro-nelsonite have magmatic evolution trends different from the gabbronorite, this is also indicated by the diagram of Sr contents versus An percentage of (Fig. 9B). This suggests that the rocks have different fractional crystallization processes due to liquid immiscibility.

Similarly positive neodymium isotope values of the Damiao gabbronorite and nelsonite/Fe–Ti oxides ore ($\varepsilon N_d = -4.0$ to -4.7 and -3.2 to -4.8 respectively) suggest insigneficant crustal assimilation during fractional crystallization (Zhao et al., 2009). It is noteworthy that the ilmenite from the Damiao gabbronorite, nelsonite and Fe–Ti oxides ore are similar in Nb and Ta (Fig. 12), but evidently lower in Ta and Nb than the Tellnes ilmenite. This also suggests a weak crustal assimilation occurred during the fractional crystallization. Thus, the occurrence of liquid immiscibility cannot be attributed to crustal contamination.

Table 4
Representative trace element geochemistry of apatite.

		ZK12-88ap	ZK12-86ap	ZK12-87ap	HB2-16ap	HB2-16ap-1	ZK12-46AP	HB12–6ap	HB12-8ap	HB2-35ap	HB12-7ap	HB12–11
		gabbronorite	gabbronorite	gabbronorite	nelsonite	nelsonite	nelsonite	nelsonite	nelsonite	gabbro-nelsonite	gabbro-nelsonite	gabbro-nelsonite
Mg	LA-ICPMS	279.22	257.12	256.44	1566.60	1441.01	524.45	686.25	1492.23	316.03	460.58	780.23
V	LA-ICPMS	10.75	10.56	8.66	5.85	7.50	11.41	4.60	2.78	5.13	3.87	5.84
Cr	LA-ICPMS	5.89	1.63	2.97	10.74	1.64	3.37	4.74	2.31	1.76	0.75	1.33
Mn	LA-ICPMS	153.68	212.48	188.03	611.29	567.10	334.54	404.07	706.93	207.05	235.81	342.55
Rb	LA-ICPMS	0.02	0.17	0.04	0.64	0.01	0.02	0.02	0.34	0.02	0.01	0.09
Sr	LA-ICPMS	510.63	545.70	547.50	1078.38	1036.54	690.35	901.79	869.27	801.55	653.31	930.33
Y	LA-ICPMS	386.61	435.24	367.90	387.24	420.70	437.36	377.98	308.69	253.73	248.89	339.63
Zr	LA-ICPMS	2.37	6.07	4.32	5.17	6.94	5.77	5.11	7.48	3.20	3.05	6.41
Nb	LA-ICPMS	0.01	0.21	0.00	0.05	0.02	0.01	0.01	0.08	0.02	0.00	0.04
La	LA-ICPMS	433.28	402.30	405.94	327.30	334.02	427.65	293.65	267.26	234.79	204.38	299.94
Ce	LA-ICPMS	1173.93	1080.52	1037.22	827.65	850.97	1062.13	715.29	635.30	590.58	522.22	736.44
Pr	LA-ICPMS	178.04	161.83	149.99	127.94	127.77	153.69	111.45	100.98	88.57	81.62	113.18
Nd	LA-ICPMS	876.00	828.22	735.37	644.32	667.59	733.55	602.40	535.70	485.55	432.59	566.79
Sm	LA-ICPMS	173.37	165.60	140.92	143.07	138.94	157.95	121.48	103.96	101.71	91.45	123.00
Eu	LA-ICPMS	13.38	17.97	20.11	37.96	37.09	34.23	30.49	26.72	25.50	24.32	30.80
Gd	LA-ICPMS	149.01	147.32	122.48	134.82	146.75	133.10	114.38	94.20	91.26	85.49	117.46
Tb	LA-ICPMS	17.69	17.25	13.99	15.46	15.77	15.96	13.18	10.68	10.10	9.32	12.65
Dy	LA-ICPMS	93.08	89.87	75.93	86.10	91.10	91.01	74.10	57.55	51.04	50.14	67.82
Ho	LA-ICPMS	14.62	16.30	12.99	15.83	16.20	16.38	13.67	11.03	9.14	8.76	12.04
Er	LA-ICPMS	35.46	46.06	32.53	38.41	40.53	40.56	42.55	33.13	23.90	23.43	30.09
Tm	LA-ICPMS	3.07	4.77	3.22	4.51	4.29	4.86	3.66	2.89	2.16	2.20	3.22
Yb	LA-ICPMS	12.59	26.12	17.26	25.82	25.45	26.20	22.22	15.84	11.75	12.30	17.14
Lu	LA-ICPMS	1.52	3.53	2.17	3.26	3.24	3.84	2.78	2.15	1.69	1.62	2.50
Pb	LA-ICPMS	2.17	1.29	1.40	1.79	1.28	1.81	1.27	1.06	0.74	0.51	1.30
Th	LA-ICPMS	14.61	6.05	7.94	1.29	1.58	2.28	1.36	1.13	0.76	0.73	1.40
U	LA-ICPMS	3.65	1.67	1.68	0.39	0.34	0.81	0.26	0.45	0.20	0.19	0.43
total REE		3175.05	3007.65	2770.13	2432.44	2499.71	2901.11	2161.31	1897.40	1727.73	1549.84	2133.06
Eu/Eu*		0.25	0.35	0.47	0.84	0.79	0.72	0.79	0.83	0.81	0.84	0.78

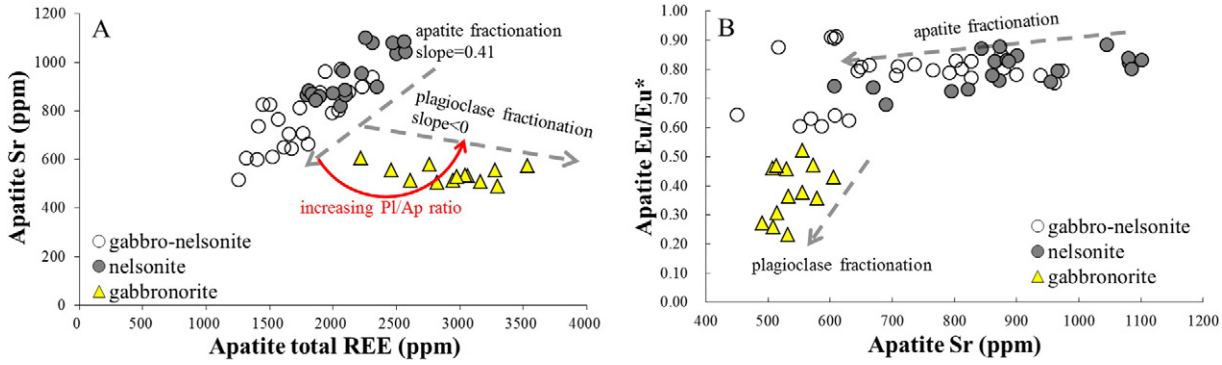

Fig. 8. A. Apatite from the nelsonite and gabbro-nelsonite contains positively correlated Sr and REEs, whereas that from the gabbronorite is negatively correlated. Strontium and REEs in the parental magma decrease proportionally only when apatite fractionate. When plagioclase fractionation dominates, Sr decreases but REEs increase slightly in the parental magma. B. Weak negative Eu anomaly is present in the apatite from the nelsonite and gabbro-nelsonite, and apatite from the gabbronorite contains distinct negative Eu anomaly. Substantial plagioclase fractionation would lead to Eu and Sr depletions in the residual magma. Chondrite values are from Sun and McDonough (1989).

6.2. Evolution of the Fe–Ti–P-rich magma, fractional crystallization and gravitational differentiation of apatite, magnetite and ilmenite

Influence of ilmenite exsolution on the Cr content in magnetite is insignificant (Table 3), and no exsolution texture occurs in ilmenite (Fig. 3A). Therefore, the Cr contents of the magnetites and ilmenites (Tables 1 and 2, Fig. 10D) indicate that the parental magma of the nelsonite and Fe–Ti oxides ore were less fractionated than those of the gabbronorite in the Damiao complex.

Both Cr and Ni are compatible for magnetite, ilmenite and pyroxene (Cawthorn and McCarthy, 1980; Namur et al., 2010; Song et al., 2013). Particularly, partition coefficient of Cr between magnetite and magma can reach 100 or above (Luhr and Carmicheal, 1980). Thus, Cr and Ni in the magma and the crystalized minerals would decrease with fractional crystallization when the amount of crystallized magnetite is above 1%. The positive correlations of Ni and Cr between magnetite and ilmenite and large content variations indicate extensive fractional crystallization of the Fe–Ti oxides (Fig. 7).

Both Sr and REEs are compatible in apatite but incompatible in magnetite and ilmenite, and thus apatite fractionation would cause Sr and REEs depletion. Fractionation of apatite and Fe–Ti oxides would result in the decrease of Sr and REEs in the residual magma and could not produce negative Eu anomaly. Fig. 8 shows that Sr is positively correlated with REEs in the apatite from the nelsonite, and there is no distinct negative Eu anomaly. This reflects that Sr was also positively correlated with REEs in the Fe–Ti–P rich magma, and suggests that apatite fractionation, not plagioclase, had dominated the fractional crystallization process. Fig. 9 illustrates that although the clinopyroxene from the gabbro-nelsonite and from the gabbronorite contains similar Mg#, the plagioclase from the gabbro-nelsonite contains higher Sr and lower An than that from the gabbronorite, suggesting significant apatite fractionation occurred in the gabbro-nelsonite prior to the plagioclase. This also indicates that the formation of the gabbro-nelsonite was after the nelsonite. Fig. 10B shows that extensive crystallization of apatite from the Fe–Ti–P rich magma may have resulted in the positive correlations between Sr and Mg in the apatite from the nelsonite. On the contrary, the negative Sr and REEs correlation for the apatite from the gabbronorite suggests that plagioclase fractionation had dominated the trace element geochemical evolution of its parental magma, and apatite fractionation may have been late. This may have produced the low Sr and the more pronounced negative Eu anomaly in the apatite from the gabbronorite (Fig. 8).

Similar Mg, Mn and Cr contents were found in the Fe–Ti oxides from the Damiao Fe–Ti oxides ore and nelsonite (Fig. 10C, D), and the transitional contact relationship between the Fe–Ti oxides ore and nelsonite indicate a continuous fractionation. Densities of Fe–Ti oxides (4.7–5.2 g/cm^3) are far higher than apatite (~3.5 g/cm^3) (Scoates, 2000). The proportion of apatite increases upwards in the large orebodies implies gravitational differentiation between magnetite/ilmenite and apatite in the Fe–Ti–P-rich magma.

7. Petrogenetic model and conclusions

Both the mantle-derived magma model (Ashwal, 1993; Bybee et al., 2014; Emslie, 1985; Kushiro and Fujii, 1977) and the lower crustal partial melting model (Duchesne et al., 1999) consider that the anorthosite petrogenesis comprises two stages: 1) primitive magma fractionates in the deep magma chamber(s), with plagioclase floating and accumulating in the magma chamber roof; 2) plagioclase and residual magma (in the form of crystal mush) rise to the shallow magma chamber(s),

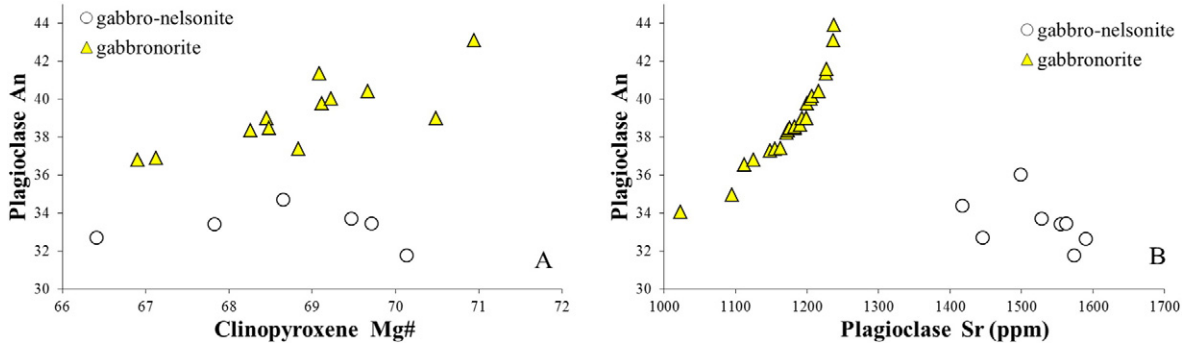

Fig. 9. A. Positive correlation between plagioclase An and clinopyroxene Mg# contents in the gabbronorite. Clinopyroxene Mg# content in the gabbro-nelsonite is similar to the gabbronorite, whilst the anhedral plagioclase An content in the gabbro-nelsonite is lower; B. Positive correlation between plagioclase An and Sr contents in the gabbronorite. Plagioclase from the gabbro-nelsonite contains higher Sr and lower An contents than the gabbronorite.

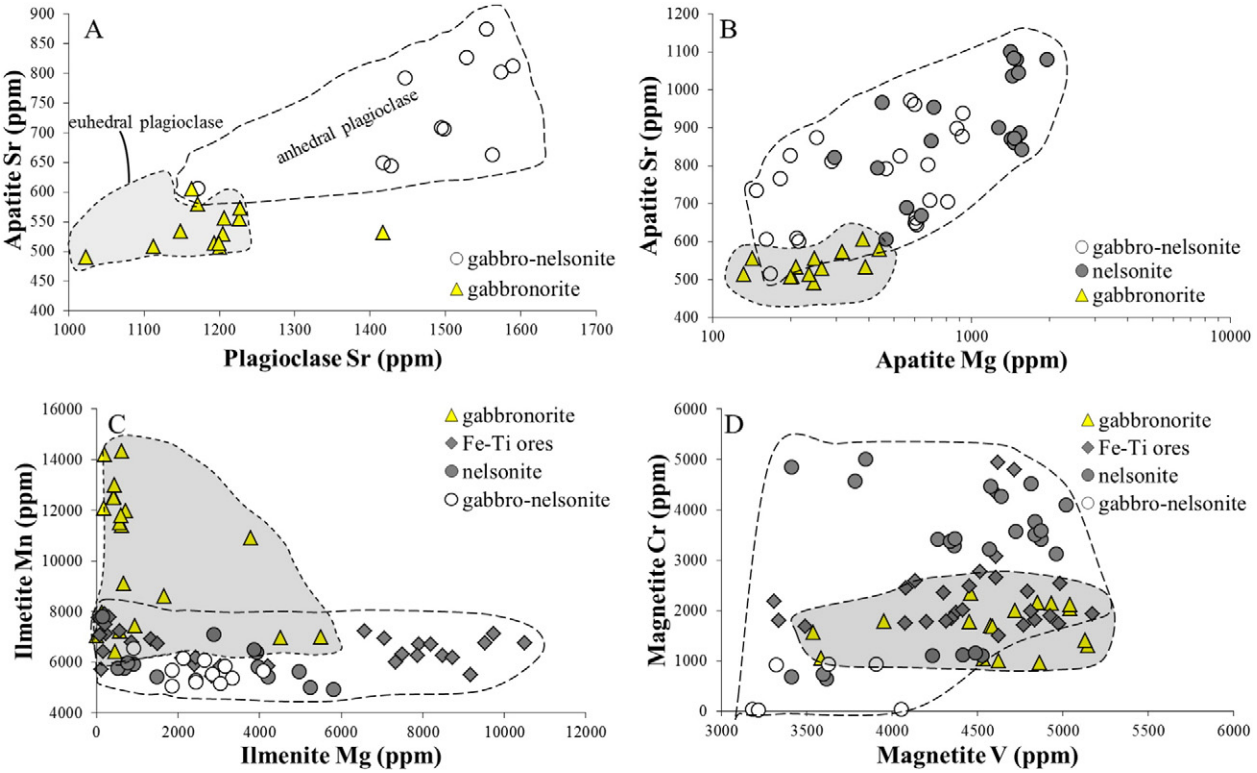

Fig. 10. Trace element geochemistry of apatite, plagioclase, magnetite and ilmenite suggests that the parental magma of nelsonite was less fractionated than that of the gabbronorite. A. Positive Sr correlation between the apatite and plagioclase from the gabbronorite and gabbro-nelsonite. Higher Sr present in the anhedral plagioclase and apatite from the gabbro-nelsonite than the euhedral plagioclase and apatite from the gabbronorite. B. Positive Sr and Mg correlation in the apatite from the nelsonite, and the Sr and Mg contents are higher than those in the apatite from the gabbronorite; C. Ilmenite from the Fe–Ti oxides ore and nelsonite contains high Mg and low Mn contents; D. Magnetite from the Fe–Ti oxides ore and nelsonite contains high Cr content.

further fractionate and form the anorthosite complexes. Charlier et al. (2010) further suggest that magma replenishment may result in two generations of anorthosite, each containing plagioclase with different An and Sr contents.

Based on field geological evidence and mineral geochemistry, we propose a new petrogenetic model for the formation of the Fe–Ti oxides orebodies in the Damiao anorthosite complex. Substantial crystallization of plagioclase and orthopyroxene of a primary magma derived from the upper mantle or lower crust may have occurred in deep-seated magma chamber(s). The plagioclase may have floated to the top of the deep-seated magma chamber, whereas the orthopyroxene settled to the bottom due to their respective densities. Extensive fractionation of plagioclase and orthopyroxene may have produced a residual ferrodioritic magma, which was REE-enriched and Sr- and Eu-depleted. The plagioclase crystal mush may have risen to the shallow magma chamber(s), where the aggregated plagioclase formed the Damiao anorthosite and the interstitial ferrodioritic magma in the plagioclase mush concentrated and formed the Damiao gabbronorite. During magma replenishments, the remaining highly evolved ferrodioritic magma may have mixed with the new primary magma to form a less evolved magma, which then separated into Fe–Ti–P-rich and SiO_2-rich magmas via liquid immiscibility, probably in a shallower depth. According to Schmidt et al. (2006) and Veksler et al. (2006), the Fe–Ti–P-rich magma is richer in REEs, Sr, Cr, Ni and V than the SiO_2-rich magma. The less dense SiO_2-rich magmas may have ascended and accumulated above the anorthosite to form the mangerite, whereas the denser Fe–Ti–P-rich magmas were squeezed into fractures in the anorthosite or along the contact between anorthosite and gabbronorite lenses. Subsequently, crystallization and gravitational fractionation of magnetite, ilmenite and apatite from the Fe–Ti–P-rich magma may have formed the Fe–Ti oxides ore in the lower- and middle parts of the steeply inclined orebodies, and the nelsonite was formed in the upper part (Fig. 1). The residual magma may have become SiO_2-rich and led eventually to the crystallization of anhedral plagioclase and clinopyroxene (Fig. 3D, E) and the formation of gabbro-nelsonite at the tops of the Fe–Ti oxides orebodies (Fig. 1). The apatite crystallized from the Fe–Ti–P-rich magma

Table 5
Calculated compositions of the magmas in equilibrium with apatite from the various Damiao rock types.

	Sr	La	Ce	Pr	Nd	Sm	Eu	Gd	Tb	Dy	Ho	Er	Tm	Yb	Lu
Average concentration in apatite (Cap)															
Gabbronorite	534.61	413.84	1097.22	163.29	813.20	159.96	17.16	139.60	16.31	86.30	14.64	38.01	3.69	18.66	2.41
Nelsonite	915.26	329.97	818.27	124.36	636.71	133.08	33.30	124.65	14.21	79.97	14.62	39.04	4.04	23.11	3.05
Gabbro-nelsonite	795.06	246.37	616.41	94.46	494.98	105.39	26.87	98.07	10.69	56.34	9.98	25.80	2.53	13.73	1.93
Partition coefficient	1.4	12	15	17	19	20	13	20	19	18	16.8	15.5	14.2	13	10
Concentration in calculated parental magmas (Cl)															
Gabbronorite	381.86	34.49	73.15	9.61	42.80	8.00	1.32	6.98	0.86	4.79	0.87	2.45	0.26	1.44	0.24
Nelsonite	653.76	27.50	54.55	7.32	33.51	6.65	2.56	6.23	0.75	4.44	0.87	2.52	0.28	1.78	0.31
Gabbro-nelsonite	567.90	20.53	41.09	5.56	26.05	5.27	2.07	4.90	0.56	3.13	0.59	1.66	0.18	1.06	0.19

A calculation of the composition of the magmas from which the apatites crystallized may be obtained by inversion of these element concentrations using the equation: Cl = Cap/D. The partition coefficients used for this calculation are from Bedard (2001).

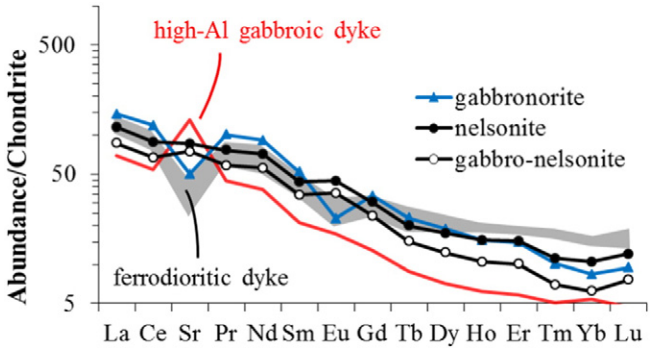

Fig. 11. Normalized trace element patterns of the magmas in equilibrium with apatite from the various Damiao rock types. Partition coefficient values are from Bedard (2001). Ferrodioritic and High-Al gabbroic dykes are from Zhao et al. (2009). Chondrite values are from Sun and McDonough (1989).

is therefore richer in Sr and shows less negative Eu anomaly than that in the gabbronorite (Fig. 8B). Additionally, the magnetite and ilmenite in the Fe–Ti oxides ore and nelsonite (from the Fe–Ti–P-rich magma) were Cr- and Mg-rich (Tables 1, 2, Fig. 10C, D). The Fe–Ti oxides and apatite in the Fe–Ti oxides orebody show significant compositional differentiation (Figs. 8, 10C, D). The residual magma may have then fractionated plagioclase and clinopyroxene, forming the Damiao gabbro-nelsonite at the tops of the orebodies.

This new petrogenetic model can explain the distribution of the Fe–Ti oxides ore, nelsonite and gabbro-nelsonite in the large-scale irregular stratiform-like or lensoid Fe–Ti oxides orebodies, as well as the sharp contact between the orebodies and anorthosite or gabbronorite. This model also explains the trace element compositional features of the apatite and Fe–Ti oxides from the Damiao nelsonite/Fe–Ti oxides ore.

Supplementary data to this article can be found online at http://dx.doi.org/10.1016/j.oregeorev.2016.05.028.

Acknowledgements

This work was funded by the National Basic Research Program of China (2012CB416804), the CAS/SAFEA International Partnership Program for Creative Research Teams — (Intraplate Mineralization Research Team; KZZD-EW-TZ-20), and research grants from SKLODG (SKLODG-ZY125-06), and NSFC (41473024 and 41373042). Drs. Lie-Meng Chen and Yu-Wei She are greatly appreciated for the helpful discussions and suggestions during the preparation of this manuscript. Special thanks are given to D. Savard from the Université du Québec à Chicoutimi (Québec, Canada) for kindly providing the Sample BC28 and helping to quality control on the trace elements in Fe–Ti oxides.

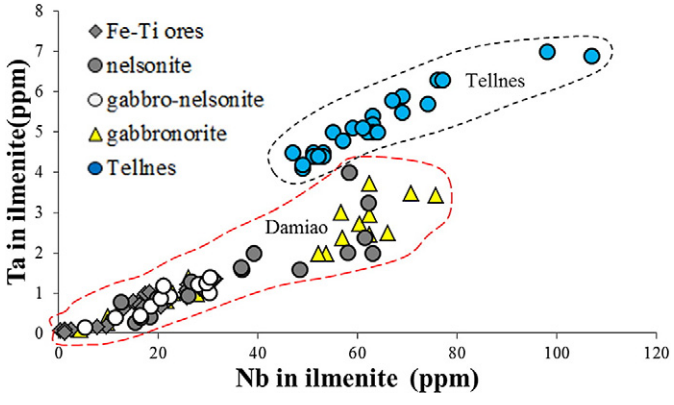

Fig. 12. Ilmenite from the various Damiao rock types contains a consistent Ta–Nb evolution trend.

References

Ashwal, L.D., 1993. Anorthosite: Minerals and Rocks, 21. Springer, Berlin, pp. 83–218.
Bedard, J.H., 2001. Parental magmas of the Nain Plutonic Suite anorthosites and mafic cumulates: a trace element modelling approach. Contrib. Mineral. Petrol. 141, 747–771.
Bybee, G.M., Ashwal, L.D., Shirey, S.B., Horan, M., Mock, T., Andersen, T.B., 2014. Pyroxene megacrysts in Proterozoic anorthosites: Implications for tectonic setting, magma source and magmatic processes at the Moho. Earth Planet. Sci. Lett. 389, 74–85.
Cawthorn, R.G., McCarthy, T.S., 1980. Variations in Cr content of magnetite from the upper zone of the Bushveld Complex. Evidence for heterogeneity and convection currents in magma chambers. Earth Planet. Sci. Lett. 46, 335–343.
Charlier, B., Grove, T.L., 2012. Experiments on liquid immiscibility along tholeiitic liquid lines of descent. Contrib. Mineral. Petrol. 164, 27–44.
Charlier, B., Vander Auwera, J., Duchesne, J.C., 2005. Geochemistry of cumulates from the Bjerkreim–Sokndal layered intrusion (S. Norway). Lithos 83, 255–276.
Charlier, B., Duchesne, J.C., Vander Auwera, J., 2006. Magma chamber processes in the Tellnes ilmenite deposit (Rogaland Anorthosite Province, SW Norway) and the formation of Fe–Ti ores in massif-type anorthosites. Chem. Geol. 234, 264–290.
Charlier, B., Sakoma, E., Sauvé, M., Stanaway, K., Vander Auwera, J., Duchesne, J.C., 2008. The Grader layered intrusion (Havre-Saint-Pierre Anorthosite, Quebec) and genesis of nelsonite and other Fe–Ti–P ores. Lithos 101, 359–378.
Charlier, B., Duchesne, J.C., Vander Auwera, J., Storme, J.Y., Maquil, R., Longhi, J., 2010. Polybaric fractional crystallization of high-alumina basalt parental magmas in the Egersund-Ogna Massif-type Anorthosite (Rogaland, SW Norway) constrained by plagioclase and high-alumina orthopyroxene megacrysts. J. Petrol. 51, 2515–2546.
Charlier, B., Namur, O., Toplis, M.J., Schiano, P., Cluzel, N., Higgins, M.D., Auwera, J.V., 2011. Large-scale silicate liquid immiscibility during differentiation of tholeiitic basalt to granite and the origin of the Daly gap. Geology 39, 907–910.
Charlier, B., Namur, O., Bolle, O., Latypov, R., Duchesne, J.C., 2015. Fe–Ti–V–P ore deposits associated with Proterozoic massif-type anorthosites and related rocks. Earth Sci. Rev. 141, 56–81.
Chen, W.T., Zhou, M.-F., Zhao, T.-P., 2013. Differentiation of nelsonitic magmas in the formation of the ~1.74 Ga Damiao Fe–Ti–P ore deposit, North China. Contrib. Mineral. Petrol. 165, 1341–1362.
Dare, S.A.S., Barnes, S.J., Beaudoin, G., 2012. Variation in trace element content of magnetite crystallized from a fractionating sulfide liquid, Sudbury, Canada: implications for provenance discrimination. Geochim. Cosmochim. Acta 88, 27–50.
Dare, S.A.S., Barnes, S.J., Beaudoin, G., Méric, J., Boutroy, E., Potvin-Doucet, C., 2014. Trace elements in magnetite as petrogenetic indicators. Mineral. Deposita 49, 785–796.
Duchesne, J.C., 1978. Quantitative modeling of Sr, Ca, Rb and K in the Bjerkrem–Sogndal layered lopolith (S.W. Norway). Contrib. Mineral. Petrol. 66, 175–184.
Duchesne, J.C., 1999. Fe–Ti deposits in Rogaland anorthosite (South Norway): geochemical characteristics and problems of interpretation. Mineral. Deposita 34, 182–198.
Duchesne, J.C., Liégeois, J.P., 2015. The origin of nelsonite and high-Zr ferrodiorite associated with Proterozoic anorthosite. Ore Geol. Rev. 71, 40–56.
Duchesne, J.C., Liégeois, J.P., Vander Auwera, J., Longhi, J., 1999. The crustal tongue melting model and the origin of massive anorthosites. Terra Nova 11, 100–105.
Dymek, R.F., 1997. On the hemoilmenite–rutile ores at St. Urbain, Quebec. Geological Society of America Abstracts with Programs vol. 20, p. 455.
Dymek, R.F., Owens, B.E., 2001. Petrogenesis of apatite-rich rocks (nelsonites and oxide-apatite gabbronorite) associated with massif anorthosite. Econ. Geol. 96, 797–815.
Emslie, R.F., 1975. Pyroxene megacrysts from anorthositic rocks: a new clue to the sources and evolution of the parent magmas. Can. Mineral. 13, 138–145.
Emslie, R.F., 1985. Proterozoic anorthosite massifs. In: Tobi, A.C., Touret, J.L.R. (Eds.), The Deep Proterozoic Crust in the North Atlantic Provinces. Reidel, Dordrecht, pp. 39–60.
Hebei BGMR, 2009. (No.4 Geological Brigade of Hebei Geology and Mineral Exploration Bureau). Research report on the Geology and genesis of anorthosite complex hosted V–Ti magnetite–apatite deposits, Chengde, Hebei province in Chinese.
Hunter, R.H., Sparks, R.S.J., 1987. The differentiation of the Skaergaard intrusion. Contrib. Mineral. Petrol. 95, 451–461.
Hunter, R.H., Sparks, R.S.J., 1990. The differentiation of the Skaergaard intrusion. A reply. Contrib. Mineral. Petrol. 104, 248–254.
Jakobsen, J.K., Veksler, I.V., Tegner, C., Brooks, C.K., 2005. Immiscible iron- and silica-rich melts in basalt petrogenesis documented in the Skaergaard intrusion. Geology 33, 885–888.
Jang, Y.D., Naslund, H.R., 2003. Major and trace element variation in ilmenite in the Skaergaard Intrusion: petrologic implications. Chem. Geol. 193, 109–125.
Kolker, A., 1982. Mineralogy and geochemistry of Fe–Ti oxides and apatite(nelsonite) deposits and evaluation of the liquid immiscibility hypothesis. Econ. Geol. 77, 1146–1158.
Kushiro, I., Fujii, T., 1977. Floatation of plagioclase in magma at high pressures, and its bearing on the origin of anorthosite. Proc. Jpn. Acad. Ser. B 53, 262–266.
Lester, G.W., Clark, A.H., Kyser, T.K., Naslund, H.R., 2013. Experiments on liquid immiscibility in silicate melts with H_2O, P, S, F and Cl: implications for natural magmas. Contrib. Mineral. Petrol. 166, 329–349.
Lindsley, D.H., 2003. Do Fe–Ti Oxide Magma Exist? Geology: Yes; Experiment: No! Vol. 9. NGU Special Publication, pp. 34–35.
Liu, Y.S., Hu, Z.C., Gao, S., Günther, D., Xu, J., Gao, C.C., Chen, H.H., 2008. In situ analysis of major and trace elements of anhydrous minerals by LA–ICP–MS without applying an internal standard. Chem. Geol. 257, 34–43.
Longhi, J., Vander Auwera, J., Fram, M., Monthieth, J.N., 1993. Pressure effects, kinetics and rheology of anorthositic and related magmas. Am. Mineral. 78, 1016–1030.
Luhr, J.F., Carmicheal, I.S.E., 1980. The Colima volcanic complex, Mexico. I. Post-caldera andesites from Volcan Colima. Contrib. Mineral. Petrol. 71, 343–372.
Morin, M., 1969. Labrieville map area, Saguenay County: Quebec Department of Natural Resources. Prelim. Rep. 141, 45.

Namur, O., Charlier, B., Toplis, M.J., Higgins, M.D., Liegeois, J.P., Vander Auwera, J., 2010. Crystallization sequence and magma chamber processes in the ferrobasaltic Sept Iles layered intrusion. Canada J. Petrol. 51, 1203–1236.
Okamoto, K., 1979. Geochemical study on magmatic differentiation of Asama Volcano, central Japan. J. Geol. Soc. Jpn. 85, 525–535.
Owens, B.E., Dymek, R.F., 1992. Fe–Ti–P rocks and massif anorthosite: problems of interpretation illustrated from the Labrieville and St-Urbain plutons. Quebec. Can Mineral. 30, 163–190.
Pang, K.N., Zhou, M.F., Lindsley, D., Zhao, D., Malpas, J., 2008. Origin of Fe–Ti oxide ores in mafic intrusions: evidence from the Panzhihua Intrusion, SW China. J. Petrol. 49, 295–313.
Pang, K.N., Li, C., Zhou, M.F., Ripley, E.M., 2009. Mineral compositional constraints on petrogenesis and oxide ore genesis of the late Permian Panzhihua layered gabbroic intrusion, SW China. Lithos 110, 199–214.
Philpotts, A.R., 1967. Origin of certain iron–titanium oxide and apatite rocks. Econ. Geol. 62, 303–315.
Prowatke, S., Klemme, S., 2006. Trace element partitioning between apatite and silicate melts. Geochim. Cosmochim. Acta 70, 4513–4527.
Qi, L., Hu, J., D Conrad, G., 2000. Determination of trace elements in granites by inductively coupled plasma mass spectrometry. Talanta 51, 507–513.
Reynolds, I.M., 1985. Contrasted mineralogy and texture relationships in the uppermost titaniferous magnetite layers of the Busheveld complex in the Bierkraal area north of Rustenburg. Econ. Geol. 80, 1027–1048.
Schmidt, M.W., Connolly, J.A., Gunther, D., Bogaerts, M., 2006. Element partitioning: the role of melt structure and composition. Science 312, 1646–1650.
Scoates, J.S., 2000. The plagioclase-magma density paradox re-examined and the crystallization of Proterozoic anorthosites. J. Petrol. 41, 627–649.
She, Y.W., Song, X.Y., Yu, S.Y., He, H.L., 2015. Variations of trace element concentration of magnetite and ilmenite from the Taihe layered intrusion, Emeishan large igneous province, SW China: Implications for magmatic fractionation and origin of Fe–Ti–V oxide ore deposits. J. Afr. Earth Sci. 113, 1117–1131.
Song, X.Y., Qi, H.W., Hu, R.Z., Chen, L.M., Yu, S.Y., Zhang, J.F., 2013. Formation of thick stratiform Fe–Ti oxide layers in layered intrusion and frequent replenishment of fractionated mafic magma: Evidence from the Panzhihua intrusion, SW China. Geochem. Geophys. Geosyst. 14, 712–732.
Sun, S.S., McDonough, W.F., 1989. Chemical and isotopic systematic of oceanic basalts: implications for mantle composition and process. In: Saunders, A.D., Norry, M.J. (Eds.), Magmatism in the Ocean Basin. Geol. Soc. Lond. Spec. Publ. 42, 313–345.
Tollari, N., Toplis, M.J., Barnes, S.J., 2006. Predicting phosphate saturation in silicate magmas: an experimental study of the effects of melt composition and temperature. Geochim. Cosmochim. Acta 70, 1518–1536.
Tollari, N., Barnes, S.J., Cox, R., Nabil, H., 2008. Trace element concentrations in apatites from the Sept-Îles Intrusive Suite, Canada — Implications for the genesis of nelsonites. Chem. Geol. 252, 180–190.
Toplis, M.J., Carroll, M.R., 1995. An experimental study of the influence of oxygen fugacity on Fe–Ti oxide stability, Phase relations, and mineral–melt equilibria in ferro-basaltic systems. J. Petrol. 36, 1137–1171.
Vantongeren, J.A., Mathez, E.A., 2012. Large-scale liquid immiscibility at the top of the Bushveld Complex, South Africa. Geology 40, 491–494.
Veksler, I.V., Dorfman, A.M., Danyushevsky, L.V., Jakobsen, J.K., Dingwell, D.B., 2006. Immiscible silicate liquid partition coefficients: implications for crystal-melt element partitioning and basalt petrogenesis. Contrib. Mineral. Petrol. 152, 685–702.
Veksler, I.V., Dorfman, A.M., Borisov, A.A., Wirth, R., Dingwell, D.B., 2007. Liquid immiscibility and the evolution of basaltic magma. J. Petrol. 48, 2187–2210.
Von Gruenewaldt, G., 1993. Ilmenite–apatite enrichments in the upper zone of the Bushveld Complex: a major titanium-rock phosphate resource. Int. Geol. Rev. 35, 987–1000.
Wang, K., Xing, C.M., Ren, Z.Y., Wang, Y., 2013. Liquid immiscibility in the Panzhihua mafic layered intrusion: evidence from melt in apatite. Acta Petrol. Sin. 29, 3503–3518 (in Chinese with English abstract).
Watson, T.L., Taber, S., 1910. Nelsonite, a new rock type; its occurrence, association, and composition. Geol. Soc. Am. Bull. 21, 787.
Watson, T.L., Taber, S., 1913. Geology of the titanium and apatite deposits of Virginia. Virginia Geological Survey Bulletin Vols. 3-A, p. 308.
Xie, G.H., 2005. The Petrology And Geochemistry Of Damiao Massif Anorthosite And Miyun Rapakivi-Granite: Involving Discussion On Distribution And Significance Of Global Massif-Anorthosite And Rapakivi Granite. Science press, Beijing (in Chinese).
Yang, J.H., Wu, F.Y., Liu, X.M., Xie, L.W., 2005. Zircon U–Pb ages and Hf isotopes and their geological significance of the Miyun rapakivi granites from Beijing. Chin. Acta Petrol. Sin. 21, 1633–1644 (in Chinese with English abstract).
Ye, D.H., Yang, Q.W., Xing, J.R., 1996. The Damiao anorthosite and vanadic-titano magnetite and apatite deposits associated with the anorthosite in Chengde, Hebei. Field Trip Guide T216, 30th International Geological Congress, Beijing, China.
Zhang, S., Liu, S., Zhao, Y., Yang, J., Song, B., Liu, X., 2007. The 1.75–1.68Ga anorthosite–mangerite–alkali granitoid–rapakivi granite suite from the northern North China Craton: magmatism related to a Paleoproterozoic orogen. Precambrian Res. 155, 287–312.
Zhao, G.C., Cawood, P.A., Wilde, S.A., 2000. Metamorphism of basement rocks in the Central Zone of the north China Craton: implications for Paleoproterozoic tectonic evolution. Precambrian Res. 155, 287–312.
Zhao, G.C., Cawood, P.A., Wilde, S.A., Sun, M., 2002. Review of global 2.1–1.8 Ga orogens: implications for a pre-Rodinia supercontinent. Earth Sci. Rev. 59, 125–162.
Zhao, T.P., Chen, W., Zhou, M.F., 2009. Geochemical and Nd–Hf isotopic constraints on the origin of the ~1.74-Ga Damiao anorthosite complex, North China Craton. Lithos 113, 673–690.
Zhou, M.F., 2005. Geochemistry, petrogenesis and metallogenesis of the panzhihua gabbroic layered intrusion and associated Fe–Ti–V oxide deposits, Sichuan Province, SW China. J. Petrol. 46, 2253–2280.